Direct Single Impinging Jet Cooling of a MOSFET Power Electronic Module

Johannes Jörg, Silvano Taraborrelli, *Student Member, IEEE*, Garikoitz Sarriegui, Rik W. De Doncker, *Member, IEEE*, Reinhold Kneer, and Wilko Rohlfs

***Abstract*—This paper presents an approach of direct liquid jet impingement cooling of a typical MOSFET power module. A single micro water jet was installed for cooling the upper surface of a MOSFET semiconductor package. In contrast to standard cooling methods, this approach focuses on hot spot removal omitting any kind of heat spreading device. The cooling chamber was directly soldered to the MOSFET cover that represents a very efficient way of liquid cooling. Two different configurations with and without electrical insulation (TIM) were used to investigate the importance of insulating material. In the range of 10–100 mL/min coolant flow rates at an inlet temperature of 22.5 °C a maximum power distribution of 51 W (at 30 mL/min) next to a maximum measured MOSFET temperature of 163 °C could be realized. Heat transfer coefficients up to 12 000 W/m$^2\cdot$ K were achieved using only 10.8 cm^3 of assembly space for the cooling device. With electrical insulation, the heat transfer coefficient exceeded 6000 W/m$^2\cdot$ K at a coolant flow rate of 30 mL/min and pumping power of 3 mW. The results illustrate the potential of direct liquid cooling using impinging microjets in combination with a compact injection chamber. The individual cooling of semiconductors offers new perspectives in the design of power electronic modules.**

***Index Terms*—Liquid cooling, power electronics, submerged jet impingement, thermal resistance.**

Nomenclature

DBC	Direct bonded copper.
CFD	Computational fluid dynamics.
GaN	Gallium nitrite.
IGBT	Insulated-gate bipolar transistor.
JBS	Junction barrier Schottky.
MOSFET	Metal–oxide–semiconductor field-effect transistor.
PCB	Printed circuit board.
SiC	Silicon carbide.
TIM	Thermal interface material.
A_M	Water covered surface area (mm^2).
D	Nozzle diameter (mm).
H	Nozzle height (mm).
I_{DS}	Drain-to-source current (A).
L_N	Nozzle length (mm).
P	Pumping power (mW).
$\dot{Q}_{\mathrm{el}}$	Electrical power (W).
R_{Adapter}	Thermal resistance of the adapter plate (cm$^2\cdot$ K/W).
R_{Jet}	Thermal resistance of the jet impingement (cm$^2\cdot$ K/W).
$R_{\mathrm{Jet+Adapter}}$	Thermal resistance of the jet impingement and adapter plate (cm$^2\cdot$ K/W).
t	Time (s).
T_I	Inlet temperature (°).
T_M	MOSFET temperature (°).
U_{DS}	Drain-to-source voltage (V).
U_{GS}	Gate-to-source voltage (V).
$\dot{V}$	Coolant volume flow rate (mL/min).
$\bar{\alpha}$	Spatially averaged heat transfer coefficient (W/m$^2\cdot$ K).
$\bar{\alpha}_{\mathrm{Jet}}$	Heat transfer coefficient of the jet impingement (W/m$^2\cdot$ K).
δ_{Brass}	Layer thickness of the adapter plate (brass) (mm).
$\delta_{\mathrm{Insulation}}$	Layer thickness of the electrical insulation (mm).
Δp	Pressure difference (mm).
λ_{Brass}	Heat conductivity of brass (W/m$\cdot$ K).
λ_{C}	Heat conductivity of the coolant (water) (W/m$\cdot$ K).
$\lambda_{\mathrm{Insulation}}$	Heat conductivity of the electrical insulation (W/m$\cdot$ K).
ν	Kinematic viscosity.
Re	Reynolds number $(-)$.
$\overline{\mathrm{Nu}}$	Average Nusselt number $(-)$.
Pr	Prandtl number $(-)$.

Manuscript received December 19, 2016; revised April 24, 2017; accepted June 12, 2017. Date of publication June 29, 2017; date of current version February 1, 2018. This work was supported by the Deutsche Forschungsgemeinschaft (DFG, German Research Foundation) within the framework of the mobilEM Post Graduate Program under Grant GRK 1856. Recommended for publication by Associate Editor S. Ang. *(Corresponding author: Johannes Jörg.)*

J. Jörg, R. Kneer, and W. Rohlfs are with the Institute of Heat and Mass Transfer, RWTH Aachen University, Aachen 52056, Germany (e-mail: joerg@wsa.rwth-aachen.de; kneer@wsa.rwth-aachen.de; rohlfs@wsa.rwth-aachen.de).

S. Taraborrelli, G. Sarriegui, and R. W. De Doncker are with the Institute for Power Electronics and Electrical Drives, RWTH Aachen University, Aachen 52066, Germany (e-mail: Silvano.Taraborrelli@isea.rwth-aachen.de; Garikoitz.Sarriegui@isea.rwth-aachen.de; post@isea.rwth-aachen.de).

Digital Object Identifier 10.1109/TPEL.2017.2720963

I. Introduction

POWER electronics have proven to fulfill the rising demands on control, energy efficiency, and reliability in an increasing number of applications throughout the last decade. For future electronic application it is assumed that all electronic power will be controlled by at least one power electronic device [1]. In power electronic applications, power loss caused by switching and conduction losses leads to extensive heat generation confined to small areas. This heat needs to be removed by adequately designed heat sinks. Heat sinks have to provide a

See http://www.ieee.org/publications_standards/publications/rights/index.html for more information.

sufficient surface area for convection, radiation, and conduction as well as take into account steady state as well as transient operating conditions. Heat sink designs focus on extensive heat spreading. In common cooling applications, heat is dissipated by conduction through base plate and heat spreader, followed by convective heat transfer via the coolant (air, water, or oil). Especially in transient operating conditions reducing the internal thermal resistance of a heat sink moderates the intensity of peak heat fluxes [1].

Considering the increasing power density in contrast to weight and space reduction of power electronic modules compact and highly efficient cooling has become mandatory. As an example, automotive powertrain systems include power densities of transistor packages with MOSFET, such as dc/dc converters, that already approach heat fluxes up to 300 W/cm^2 [2].

A. State-of-the-Art Systems and Future Challenges

Today's power electronic and semiconductor devices as well as the future trends are reviewed by Benda [3] and Vobecky [4]. By focusing on fundamental physical limits, these works discuss the most important power semiconductor devices and possible future application. The authors point out that standard electronics, in general, and high-power electronics, in particular, will utilize silicon switching devices. While for the voltage range of 1–3 kV IGBT may remain the most important switching devices the voltage range below 330 V may be dominated by power MOSFETs. Power electronic modules using IGBTs, especially in combination with SiC or GaN Schottky or JBS diodes, can handle higher junction temperatures. However, the operating temperature of power electronic modules and its semiconductors should not exceed the critical temperature level for save operations of 175 °C [5].

Today's commonly used cooling solutions are listed as follows:

1) air-cooled heat sinks (natural and forced convection);
2) liquid cold plates (single and double-sided cooling);
3) microchannel coolers;
   a) liquid coolers built into the base plate;
   b) liquid coolers integrated within the DBC substrate;
4) direct contact liquid cooling of the module base plates or DBC substrate;
5) jet impingement cooling of the module base plates;
6) two-phase liquid cold plates (phase change of a dielectric refrigerant coolant at constant temperature).

Especially in the automotive sector, additional requirements for power electronic cooling have to be taken into account. In hybrid cars, e.g., compact packaging and cost limits, as well as the interconnection of peripheral components such as installed cooling cycles have to be considered. This results from the fact that the temperature of the supplied coolant is in the order of 90 °C. Here, the difference between inlet and outlet temperature of the power electronic cooling system has to be sufficiently low to prevent from coolant boiling. Schulz-Harder [6] and Saums [7] have provided a summary on state-of-the-art cooling solutions for power electronic modules in automotive applications focused on thermal management.

Deeper insights into these challenges of power modules' thermal management are presented in Leslie [8]. In addition to the high coolant temperature level the temperature difference between the die (e.g., IGBT or MOSFET) and the coolant should not exceed 30 °C. This ensures high-dissipating heat fluxes whereas the IGBT or MOSFET is held below the maximum operating temperature.

Besides temperature range, the required coolant pumping power should be considered. Pumping power, represented by the pressure drop of the heat sinks, is an important indicator of the efficiency of the cooling device. Leslie [8] compared two different cooling concepts: pin fin and microchannel cooling. The author specifically points out the difference of two common flow arrangements (parallel or normal to the heat generation surface) regarding the subsequent pressure drop and cooling performance. Contrary to parallel flow concepts, normal flow heat sinks that are associated with lower pressure drops often necessitate short flow passages. This highlights that high-performance cooling concepts also depend on a small pressure drop and low thermal resistance in the heat flow path.

A promising approach to a compact and highly efficient cooling system is represented by microchannel cold plates, such as, e.g., presented by Valenzuela and colleagues [9]. Microchannel cold plate designs focus on the integration of a normal flow configuration into an IGBT module and eliminate the necessity of a heat spreader and TIM. Instead, the microchannel cooler is directly soldered to the direct copper bonded (DCB) device. It is thus characterized by very low thermal resistance and moderate pressure drop. Using a microchannel cold plate cooler results in very high heat dissipation rates (300 W/cm^2) with a temperature difference below 50 °C. This illustrates the high potential of normal flow configurations in combination with the reduction of thermal resistance.

A thermohydraulic comparison of two liquid cooling devices under real application conditions is given by Robinson [1]. This work contrasted the performances of jet arrays and microchannels. Furthermore, the required pumping power for a desired heat removal rate was considered to illustrate the possible operating costs of each approach. Both cooling devices have to dissipate a heat flux of 250 W/cm^2 while the temperature of the power electronics (heated surface) is kept below a temperature of 85 °C. The analysis focused on heat transfer coefficients, pressure drop, and pumping power of both cooling strategies. Pumping power was limited to 0.1 W, which restricted the maximum flow rate and, accordingly, the pressure drop. The flow rates of both cooling strategies were adjusted to dissipate the mentioned heat flux and the hydraulic diameter of the microchannels, as well as the configuration of the jet arrays (number of jets and distances among them), were optimized.

Robinson [1] could show that microchannel coolers, which are known for high pressure drops, have to be operated at small coolant flow rates to meet the restrictions of low pumping power. Performance levels of the microchannels indicate that the heat transfer coefficient is strongly influenced by channel width and that it decreases with the hydraulic diameter. Raising the flow rate through microchannels will increase heat transfer but also pressure drop and, therefore, pumping power. In contrast,

impinging jet coolers can achieve high coolant flow rates due to their lower pressure drop. Here, the heat transfer coefficient also increases with flow rate. In addition, for fixed nozzle diameters and a constant total flow rate the heat transfer coefficient decreases with a larger number of jets. In contrast to a worse heat transfer coefficient, a large number of impinging jets decreases the pressure drop and, thus, the required pumping power. Concluding, under comparable operating conditions, the heat transfer coefficient of impinging jets is significantly higher compared to microchannel coolers [1].

Highlighting the challenges concerning reliability and maintenance in the automotive sector Robinson [1] further states that lower operating pressure decreases the risk of leakage. At the same time, high flow rates lead to a more uniform temperature across the cooled surface of the electronic component. Valenzuela and colleagues [9] anticipated that power devices using SiC or GaN semiconductor technologies, operated at higher switching frequencies and currents, will exceed heat generation rates of 500 W/cm^2 and further improvements of the cooling concepts are required.

In order to overcome the theoretical maximum heat removal rate of liquid coolants phase changing concepts can provide a possible solution. One promising cooling concept is presented by Levett and colleagues [10]. The authors reviewed experimental results of IGBT modules equipped with a cold plate and a vaporizable dielectric fluid. The results show that the main cooling effect is based on the liquid-to-gas phase change of common refrigerant such as R134-A. As long as the two-phase fluid runs liquid through the cold plate, the temperature level stays close to the refrigerant boiling temperature. At a flow rate of 350 mL/min a power distribution of 1 kW is achievable. Thus, low flow rates, small pumps, and reduced diameter tubes can be used. However, as a disadvantage in contrast to typical coolant concepts, such a phase change cooling concept includes the usage of a greenhouse gas (R134-A).

B. Submerged Impinging Jet Cooling Concepts

Over the last decades, impinging jet cooling has been extensively studied. Focusing on single-phase liquid jets, these studies have provided a wide range of experimental, theoretical, and numerical analyses of different impinging jet configurations [11]–[13]. The investigations range from single submerged jets [14], to multiple submerged jets [15], and impinging jet cooling of electronic modules [16].

The wide range of impinging jet configurations and their cooling performance in real applications is presented by the following studies.

A performance investigation of a submerged single-phase direct liquid-jet-impingement cold plate using a large number of impinging jet nozzles and water as a coolant is given by Brunschwiler and colleagues [17]. For nozzle diameters between 25 and 126-μm pressure drop, heat transfer coefficient, and heat removal rates were investigated feeding up to 50 000 nozzles cooling a chip area of 400 mm^2. The results show that a maximum heat transfer coefficient of 87 000 W/m$^2\cdot$K could be achieved using a nozzle diameter of 43 μm and requiring a coolant flow rate of 2.5 L/min. The small dimensions of the treelike manifold and inlet nozzles cause a pressure drop of 0.35 bar. In summary, the authors demonstrate an impressive cooling performance, however, at a cost of high pressure drop.

A reliability and performance study on an impinging jet heat exchanger design using water-ethylene glycol (mixture by volume: 50%–50%) is presented by Narumanchi and colleagues [18]. Within the context of a commercially used inverter for electric vehicle applications a channel flow-based cold plate is compared to an impinging jet heat sink. Based on experimental and numerical investigations, the results show that in comparable coolant flow ranges (approximately 10 L/min) the thermal resistance of the impinging jet configuration is 34% lower compared to the channel flow-based cold plate, the temperature uniformity significantly decreases, and the specific power increases by 82%. Further improvements are achieved using a microfinned base plate for the impinging jet cooling (34% in thermal resistance, 0.15 °C of temperature uniformity, and 118% in specific power). After 6 month contentious reliability testing no significant regression of the thermal performance of the impinging jet heat exchange, with and without microfins, is reported. Apart from supporting the superiority of impinging jets' cooling performance, the results also support the durability of heat sinks using liquid impinging jets.

Common problems of jet arrays are the interaction of surrounding nozzles with the impingement as well as coolant cross flows. Depending on the position of the outlet nozzles coolant cross flow perpendicular to the impingement direction can redirect the impinging jets in downstream direction. Both effects, jet interaction and cross flow, can inhibit fully developed wall jets and, thus, decrease the heat removal rate of the impinging jet heat sink. In their study, Han and colleagues [19] present a hybrid microcooler, which combines microjet array impingement with microtrenches for drainage. These microtrenches are used to achieve fully developed impinging jets for all individual nozzles. The hybrid microcooler is fabricated by bonding two silicone plates together and etching processes. The nozzles have a diameter of 100 μ m and the microtrenches have a width of 150 μm. Overall, more than 300 nozzles and 180 trenches are implemented into the heat sink for cooling an area of around 50 mm^2. For a coolant flow rate of 300 mL/min a pumping power of 0.05 W is required to achieve heat transfer coefficients in the range of 13 000 W/m$^2\cdot$ K. In conclusion, the authors can demonstrate that the heat transfer performance of the impinging jets can be improved by the use of microtrenches, and by this, the amount of nozzles can be reduced.

Finally, Gould and colleagues [20] present a high heat flux jet impingement cooled heat exchanger designed for harsh operating environment (e.g., underhood installation in heavy duty electrified vehicles). The heat exchanger was applied to a 600 V/50A silicon (SiC) power module and optimized by experimental studies. The authors compared the impinging jet cooling heat sink with two commercial heat sinks (liquid-cooled heat sink with meandering copper tube and microchannel cooler). Using a mixture of water-ethylene (50%–50%) as coolant, a flow rate of 195 mL/min and device junction temperature limit

of 175 °C the commercial heat sinks proofs to be insufficient. In a worst case scenario with 151 W heat load the junction temperature increases up to 290 °C for the copper tube heat sink and up to 215 °C for the microchannel heat sink. The optimized impinging jet heat sink reduces the junction temperature to 169 °C using the same coolant flow rate. The results in pressure drop and heat removal rate indicate that the best cooling performance can be achieved by one jet per heat source. With an operation time of up to 50 h, this work highlights the long-term reliability of impinging jet heat sinks. It can further be stated that heat removal rates beyond 350 W/m^2 can be realized, even in harsh environments.

C. TIM and Direct Cooling

Regardless of the employed cooling concept internal thermal resistance of the semiconductor and the TIM becomes a dominating obstacle in improving overall cooling performance. Narumanchi and colleagues [21] have stated TIMs to be even the main bottleneck to realize high heat flow rates from an IGBT or MOSFET into the coolant. In the automotive sector, a compact design of a power electronic module relies on the each component's performance. Especially for the three main components, heat spreader, heat exchanger (microchannel or impinging jet cooler), and TIM, the main performance measures consist of their reliability, high heat removal performance, and cost efficiency. Therefore, the reduction of the TIM thermal resistance is a promising approach to achieve these goals.

Taking into account numerous limiting conditions, e.g., a maximum coolant temperature of 105 °C and the temperature limitations of the device, Narumanchi and colleagues [21] investigated different electronic devices (conventional silicon-based, SiC-based, and IGBT) in combination with several TIM materials and thicknesses. The results of this study show that the thermal resistance of the investigated materials achieves a minimal value of 0.33 cm$^2 \cdot$ K/W. The thicknesses of the tested TIM layers (bond-line thickness) are 100 μm or thinner. In contrast to heat spreader, base plate, or heat sink, any of the thin TIM layers significantly increases the overall thermal resistance. Thus, for extremely compact and high performance power electronics the usage of any kind of TIM should be avoided.

Direct cooling of a power electronic modules fulfills this requirement. The cooling fluid is guided directly inside the baseplate of the module. Compared to the systems discussed above, direct cooling reduces the distance between heat generation location and dissipating surface. Thus, thermal resistance can be reduced and efficiency is increased. This is supported by the results of Schulz-Harder and colleagues [22], who focus on the benefits of replacing a standard air-cooled heat sink with TIM by a liquid-cooled base plate and jet impingement cooling. The results illustrate the negative influence of the TIM on overall thermal resistance, as well as the heat sink performances. The authors conclude that changing from air cooling to direct liquid cooling leads to significant reduction of thermal resistance between the semiconductor and the coolant.

Despite the obvious disadvantages caused by TIMs, their usage cannot be avoided if a water-based coolant is used and electrical insulation is required. However, new technologies and materials enable certain improvements of TIMs.

Engelmann and colleagues [23] focus on the experimental investigation of thermal resistances under real application conditions. This study includes solid materials (e.g., Al_2O_3 ceramic), elastomeric materials (e.g., Gap PAD 1500) as well as thermal greases (e.g., Akasa Silver Compound 450). The used test setup consisted of a surface mounted MOSFET pressed on a heat sink. The applied MOSFET was a DirectFET (L8 package).

The results of this study show that elastomeric TIMs lead to thermal resistances below 10 K/W, while solid TIMs (e.g., Al-oxide) provide further reduction of the thermal resistance. The best results (below 5 K/W) are achieved with the combination of solid TIMs with thermal greases and phase-changing materials.

Furthermore, the authors highlight the influence of the mechanical boundaries as a limiting factor to the heat removal rate of a heat sink. The measurements of the pressure distribution on the DirectFETs of a dc/dc converter pressed against a planar aluminum heat sink indicate nonhomogeneous heat conductivity between the DirectFET and the planar base plate of the heat sink. This poses an additional caveat that has to be considered when all semiconductors of a power electronic module are cooled by one base plate.

In summary, pumping power, pressure drop, and total thermal resistance are key characteristics when designing an efficient and compact power electronic cooling device. Related to the pumping power, small coolant flow rates in combination with low pressure drops result in small power consumptions and high efficiencies. Low thermal resistance can be realized by increasing corresponding heat transfer coefficients and removing material layers in the heat flow path. Overall, a designer of a power module and its cooling device has to take into account several tradeoffs when selecting an adequate heat sink: the type of coolant and coolant flow rate, pressure drop and thermal resistivity, compact size, and low weight, as well as the cost and reliability [8].

D. Direct Single Impinging Jet Cooling

Common impinging jet concepts, such as those presented in Section I-B use a large number of small and short orifice-type nozzles to generate jet impingement. A high number of nozzles and small diameters come along with disadvantages, such as high production efforts and challenging technologies for the manufacturing and maintenance. As new contribution to direct liquid jet cooling, the present study uses one single nozzle with larger diameter. Hereby, the design of the injection manifold is simplified and the size of the heat sink is reduced.

Furthermore, the study applies one long tube nozzle, offering benefits regarding hot spot removal and heat transfer rates. As shown before by our group, the velocity profile has a significant influence on local Nusselt number in the stagnation region of the impinging jet [24]. For the same Reynolds number (identical flow rate), a parabolic velocity profile emerging from the cooling nozzle exhibits a much higher capability for heat removal than a uniform velocity profile. While long tube nozzles offer enough hydraulic length to form a fully developed velocity profile of parabolic shape orifice-type nozzles induce uniform velocity profiles.

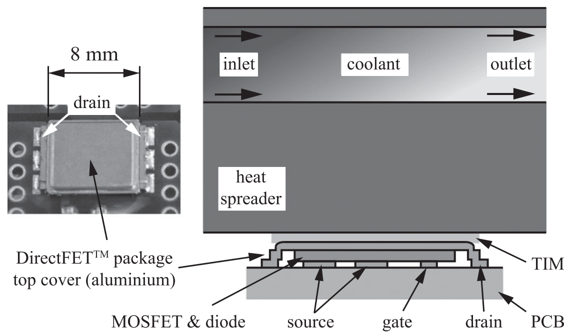

Fig. 1. Left picture shows the DirectFET Power MOSFET package mounted on a PCB. The right panel displays a schematic cross section of the DirectFET package equipped with a standard plate cooler and TIM.

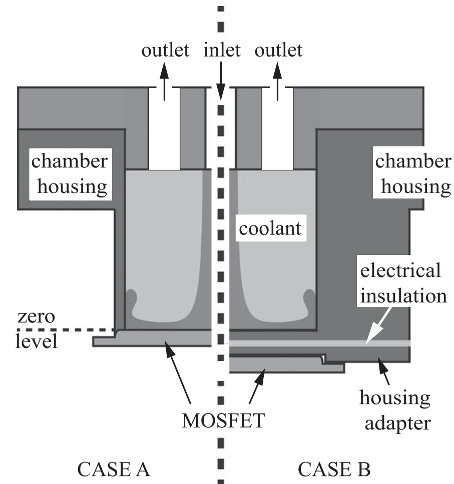

Fig. 2. Cross section of the two investigated cases, differing in the mounting to the MOSFET. Case A (left side): Thin wall chamber housing directly soldered to the MOSFET top surface. Electrical conduction between MOSFET drain and coolant. Case B (right side): Thick wall chamber housing (due to fixing screws) including an electrical insulation layer, mounted on top of a housing adapter. This adapter is soldered to the top surface of the MOSFET. In this case, there is no electrical conduction between MOSFET drain and coolant.

Instead of mounting a PCB on the cooled base plate, heat spreader, and heat sink, a single MOSFET semiconductor is cooled by a directly attached single cooling chamber. This sets way for new possibilities in the design and layout of power electronic modules due to the separate cooling of each MOSFET. Fig. 1 illustrates the experimental setup.

The MOSFET, used as switching device of a dc–dc converter, is mounted as DirectFET Power MOSFET package [25] on a PCB and is cooled by a common cold plate. Fig. 1 left panel illustrates the aluminum metal cover of the DirectFET package as well as its dimensions. Fig. 1 right panel illustrates the cross section of the DirectFET package equipped the plate cooler. The DirectFET consists of bottom connections for the gate and source supply, diode, and MOSFET in the center and drain via the top cover. The package height is below 0.5 mm. The standard heat sink for this application consists of a liquid-cooled heat sink with meandering copper tube, comparable to the heat sink investigated in [20]. It consists of a cooper base plate (heat spreader) and tube for the coolant flow. The heat sink is pressed against the MOSFETs of the converter with TIM in between.

The study presents first results on the heat dissipation performance of this approach. Taking into account the challenges for a compact, reliable, and highly efficient heat sink the presented cooling device is attached directly to the MOSFET top cover, thereby meeting the demands stated by Brunschwiler and colleagues [17] who have suggested this low-temperature bonding process. The setup further uses single microjets, well-known for high heat transfer coefficients. This setup offers the opportunity to minimize the travel path length of the heat and, thus, ends up in extremely compact chamber housing.

As illustrated in the cross sections of Fig. 2, the study includes two different test setups. The setup that is electrically noninsulated (Case A) is used to determine the upper limits of the presented impinging jet cooling device. As the coolant is in direct contact with the top cover of the MOSFET, the thermal resistance of the heat sink only depends on the heat transfer coefficient. The second setup (Case B) is equipped with an insulation layer and mounting adapter to guarantee electrical insulation between the cooling cycle and the power electronic module.

The remainder of this article is structured as follows: Section II outlines the concept of direct liquid jet cooling in the experimental setup. Section III provides a detailed insight into the phenomena taking place on the MOSFET surface and inside the cooling chamber; the focus here is on fluid dynamics and heat transfer analysis. Section IV consists of six sections. First, infrared measurements of the MOSFET top cover during the heating phase are discussed, illustrating the spatial heat generation of the MOSFET. The second and third sections address the influences of nozzle length on pressure drop, pumping power, and heat transfer coefficient. In addition, the electrically noninsulated (Case A) and electrically insulated (Case B) setups are compared regarding their heat transfer performance. Nusselt correlations for both setups are presented in comparison to fundamental research results on impinging jets. Furthermore, a detailed insight into the thermal resistance of the two setups highlights the drawback of the additionally used electrical insulation layer. Section IV presents a failure scenario, in which a break-down of the coolant supply is examined. It highlights the thermal response in case of potential shutdown of the coolant flow. Section IV-F evaluates the efficiency of the impinging jet cooling approach and compares the required pumping power to the achieved heat transfer coefficient. Section V concludes the study.

II. Experimental Setup

The experimental setups used to examine the effect of direct liquid cooling of a MOSFET (DirectFET [25]) is shown in Figs. 3–6.

The core unit consists of a 12 mm $\times$ 10 mm cooling chamber, which is 9 mm in height (shown in Fig. 3). The chamber itself is made of brass, and comprises a chamber housing and a separate top cover (both connected to each other by four removable screws). The MOSFET and chamber housing were brazed jointly in one single step onto the PCB in a brazing furnace. The advantage of this manufacturing process is that the electrical contacts will not be affected due to a second brazing stage. Furthermore, the material connection is water-proof and allows for small unit size. The separate top cover of the cooling

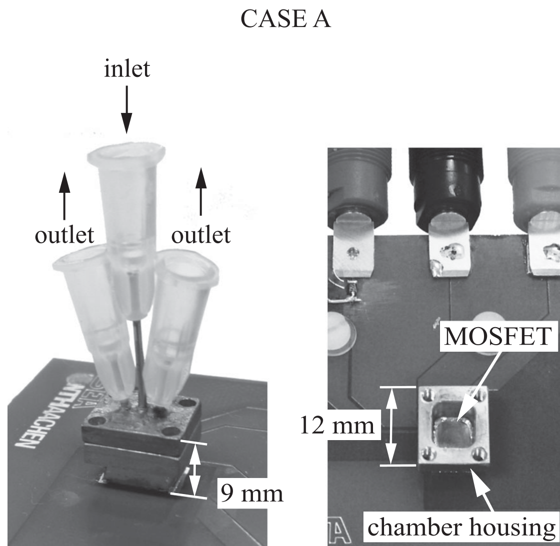

Fig. 3. Left picture depicts the electrically noninsulated cooling chamber (Case A), comprising injection and outlet nozzles, as well as electrical connection. The right picture shows the inside of the cooling chamber and the top cover of the MOSFET. This setup was used for the IR-thermography measurements.

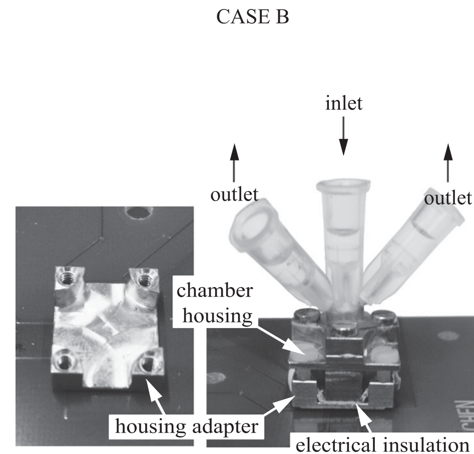

Fig. 4. Pictures of the investigated injection chamber housing, additionally equipped with an adapter plate (Case B), electrical insulation (TIM), and slightly changed housing outline. The left picture depicts the housing adapter soldered onto the MOSFET, the right picture illustrates the completely mounted single jet cooling chamber.

chamber contains three holes with a diameter of 0.9 mm each. The center hole is used for cooling supply through a $L_N = 12$ mm or $L_N = 24$ mm long cooling nozzle. The inner diameter of all nozzles is $D = 0.6$ mm. The inlet height is $H = 3$ mm above the heat transferring surface (DirectFET top cover (CASE A) or cooling chamber bottom surface (CASE B)). The shape and length of the cooling nozzle influences the emerging velocity profile of the cooling liquid and, hence, the local heat transfer. To remove the cooling liquid from the chamber the two additional holes include short outlet pipes of same diameter, but at a length of 10 mm. The prototype cooling nozzles were taken from dental medical supplies and have large connectors (yellow plastic), allowing for a simple connection to a flexible hose system. The nozzles are glued to cooling chamber cover. In real-life applications, these connectors can be of much smaller size. The electrically noninsulated setup (Case A) was used to determine the influence of the jet impingement parameters regarding the cooling performance of the device. To exclude convective and conductive heat dissipation to the surroundings, i.e., through the PCB and chamber housing outer surface, the entire experimental setup is thermally insulated. Thus, the cooling performance is determined only of the direct impinging jet cooling. This procedure is employed in both test cases.

The electrically insulated setup (Case B) is shown in Fig. 4. To ensure a certain proximity to real-life applications, the second setup includes a layer of electrical insulation. Therefore, the chamber housing could not be directly soldered onto the MOSFET top cover. Instead of the chamber housing, a housing adapter was placed on top of the MOSFET and brazed jointly to each other in the soldering furnace. This procedure enables preassembling of MOSFET + PCB + adapter. Also, the entire cooling cycle (piping, chamber housing, etc.) can be assembled separately from the electrical devices. Because it holds additional plastic mounting screws the size of the chamber housing slightly increased. Due to high thermal conductivity and insufficient thickness the thermal resistance of the soldering layer is negligible.

The pre-assembled MOSFET, PCB, and housing adapter are shown in the left picture of Fig. 4. The completely mounted cooling device is presented in the right picture. In between the housing adapter and chamber housing a thin layer of the electrical insulation pad (Gap PAD [26]) is visible. The thickness of the insulation pad consists of approximately 200 μm. Taking into account its thermal conductivity of 5 W/m· K the effective heat transfer coefficient is approximately 2.5 W/cm^2· K. Compared to the thermal conductivity of the brass (around 120 W/m· K) and the aspired goal of 300 W/cm^2 dissipated heat fluxes the additional insulation pad with its low heat transfer coefficient was expected to significantly contribute to the thermal resistance of the cooling device.

The two different test cases (Case A and Case B) allow for a separation of the aspects attributed to the impinging jet heat transfer from the aspects related to TIM and heat spreading. To compare the results of the electrically noninsulated setup (Case A) to the electrically insulated setup (Case B) the inner design of both cooling chambers is identical (top cover as well as nozzles positions are identical). Thus, the flow and convective heat transfer characteristics of both test setups are equivalent.

Fig. 5 provides an overview of the main elements of the cooling system. Fed by the inlet manifold, the coolant leaves the center nozzle perpendicular to the MOSFET surface and impinges at the center of the planar aluminum top cover. It then rebounds sideways and accelerates along the surface. The MOSFET generates heat, which is removed by the wall jet. Thus, the coolant flow heats up along the bottom of the cooling chamber and is redirected upward by the chamber wall. Besides the convective heat transfer on the lower surface an additional cooling effect could be represented by heat loss via the chamber walls and top cover. Also, mixing of the hot rebounded coolant and the remaining fluid inside the cooling chamber can occur. Finally, the

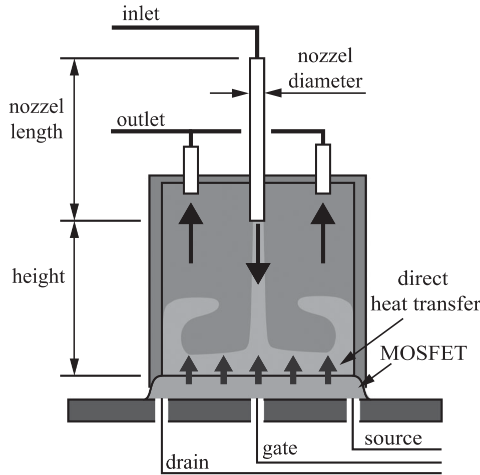

Fig. 5. Schematic display of the investigated injection chamber for direct impinging jet cooling as well as dimensions and electrical connections. The heat loss of the MOSFET is directly dissipated by the impinging jet.

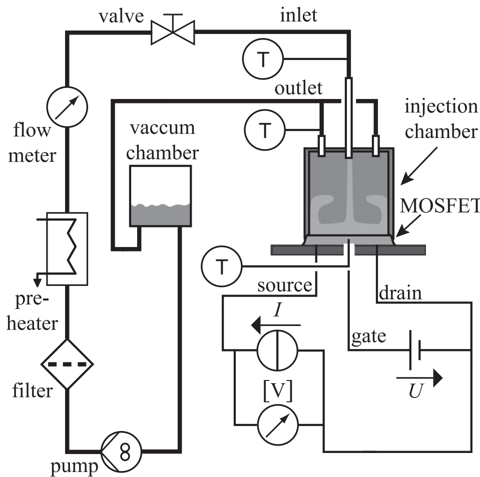

Fig. 6. Schematic display of the cooling circuit, measurement, and electrical setup. Both cooling chamber setups (with and without electrical insulation) were supplied by this experimental periphery.

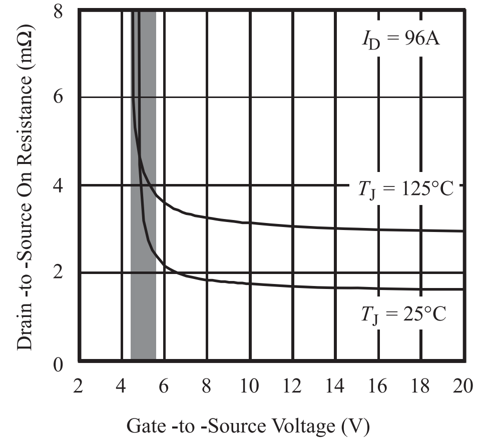

Fig. 7. Typical on-resistance versus gate voltage of the investigated MOSFET [25] for a drain-to-source current of $I_D = 96$ A and junction temperatures of $T_J = 25$–$125\ ^\circ$C. The scope of experiments is highlighted by the gray-shaded area.

coolant exits through the outlet nozzles. For both nozzle lengths (12 mm and 24 mm), the distance between the injection nozzle and the heat dissipating surface (height) is 4 mm.

The entire cooling circuit is presented in Fig. 6 and consists of a reservoir for liquid storage, from which the liquid is pumped (adjustable gear pump Gather Industrie PM8060) through a filter, a preheater (HAAKE AC 200), and a flow meter (PKP DTH08) to the cooling chamber. Special attention was paid to highly accurate flow rate measurements, for which a calorimetric flow meter was employed. The coolant flow rate is adjusted by a high precision valve. Based on liquid flow rate $\dot{V}$, nozzle diameter D and kinematic viscosity of the fluid ν, the dimensionless Reynolds number is given by

$$\mathrm{Re} = \frac{\dot{V} \cdot D}{\nu \cdot D^2 \cdot \frac{\pi}{4}}. \tag{1}$$

For future applications, the temperature levels of the inlet and outlet coolants are of great interest. Especially for a series connection of several cooling chambers the temperature difference across one cooling device needs to be determined. Immediately prior and after the cooling chamber inlet and outlet temperatures are measured using a Type-K thermocouple. The temperature of the MOSFET is measured at the bottom surface of the semiconductor. A probe hole was drilled through the PCB base plate and the tip of thermocouple is pushed from below against the MOSFET surface. The electrical circuit comprises of an adjustable power source (current controlled) that imposes a defined gate-to-source current. The electric power input of the MOSFET is given by

$$\dot{Q}_{\mathrm{el}} = U_{\mathrm{DS}} \cdot I_{\mathrm{DS}} \tag{2}$$

whereby the drain-to-source voltage U_{DS} and the respective current I_{DS} are continuously monitored during the experimental runs. A second power source is applied to control the gate voltage of the MOSFET, which allows for a precise regulation of the electrical loss of the MOSFET. The relation between the electrical resistance and the gate-to-source voltage for different temperatures is shown in Fig. 7.

The applicable voltage level of the cooling approach is restricted by the electrical insulation. Since in Case A the coolant (water) is in direct contact with the drain of the DirectFET package the applicable voltage level depends on the electrical conductivity of the coolant. In Case B, the applicable voltage level depends on the electrical conductivity of the TIM. The used Gap PAD [26] has a dielectric breakdown voltage of 5000 V. For the experimental investigations, the drain-to-source voltage U_{DS} did not exceed 30 V.

III. Fluid Dynamics and Heat Transfer Characteristics

This study focuses on the investigation of a small-scale and compact cooling device of a single MOSFET semiconductor. The heat generating area and, thus, the surface for the convective heat transfer is extremely small. The water-covered surface area A_M is confined to the bottom surface of the cooling chamber. For the first test setup (Case A), it is equal to the water-covered

area of the MOSFET top surface (right picture of Fig. 3), with a value of 40 mm^2. To provide a reasonable comparison of the two test setups, the water covered surface area A_M for the second setup was defined the same way and, thus, features the same value. The dissipated heat is defined by the power loss of the MOSFET, induced by low gate-to-source voltages U_{GS}. The gate-to-source voltage ranges between 4.58 and 4.74 V, leading to sensitive changes in resistance as given in Fig. 7. The heat loss of the MOSFET is presented by the electrical power density $\dot{Q}_{\mathrm{el}}$, as a function of the drain-to-source current I_{DS} and drain-to-source voltage U_{DS}.

Based on the temperature of the MOSFET, the water covered surface A_M, the electric power density $\dot{Q}_{\mathrm{el}}$, and the inlet temperature of the cooling liquid the spatially averaged heat transfer coefficient is determined by

$$\bar{\alpha} = \frac{\dot{Q}_{\mathrm{el}}}{(T_{\mathrm{I}} - T_M) \cdot A_M}. \tag{3}$$

This heat transfer coefficient can be translated to the dimensionless Nusselt number

$$\overline{\mathrm{Nu}} = \frac{\bar{\alpha} \cdot \mathrm{D}}{\lambda_{\mathrm{C}}} \tag{4}$$

where λ_C is the thermal conductivity of the cooling liquid. Based on these equations the performance of the cooling system will be determined in the following sections. Further analyses of the fluid dynamics inside the cooling chamber are provided by the results of the numerical investigations.

IV. Results

In the first part of this chapter, the local heat generation of the investigated type of MOSFET is analyzed using IR-thermography (see Section IV-A). In Section IV-B, the pressure drop and required pumping power are discussed based on numerical simulation results of the respective cooling system. In Section IV-C, the heat transfer characteristics of the respective chamber setup (Case A and B) are discussed and Nusselt number correlations are presented.

In Section IV-E, a shutdown scenario of the cooling cycle illustrates the failure behavior of the cooling device. Finally, Section IV-F evaluates the cooling efficiency, highlighting the heat removal drawback of the TIM.

A. Local Heat Generation of the MOSFET

In the design process of the cooling system heat generation of the MOSFET (DirectFET) was analyzed by IR-thermography. The MOSFET package (see Fig. 1) including the chamber housing of the first test setup (electrically noninsulated, Case A) was placed in front of an IR-thermography camera (Infra Tec Image IR5325), as shown in Fig. 3 (right picture). Connected to a power supply and gate voltage the IR-images of the MOSFET top cover surface were recorded during the early heat up (time span of 0.5 s after initiation). Results of the IR-measurements are shown in Fig. 8. The MOSFET was operated on a low gate-to-source voltage of $V_{\mathrm{GS}} = 4.58$ V. A drain-to-source current of $I_{\mathrm{DS}} = 1$ A was applied together with a nonpowered MOSFET while

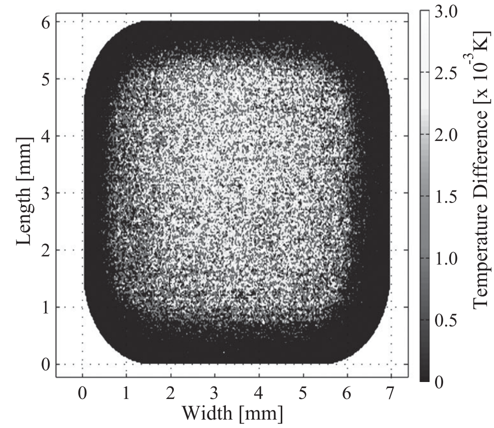

Fig. 8. Distribution of the MOSFET surface temperature change after 0.01 s of heating. The heat dissipation is caused by the power loss of the semiconductor, operated on low gate-to-source voltage V_{GS}.

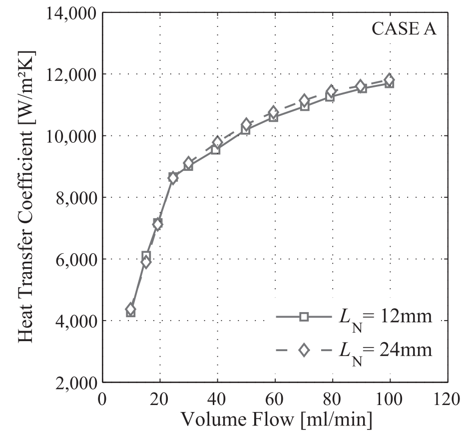

Fig. 9. Influence of the nozzle length and coolant flow rate on the spatially averaged heat transfer coefficient of the cooling chamber without electrical insulation (Case A).

documenting the measurement with an IR-camera. A frame rate of 300 Hz yielded a temperature difference for the first 0.01 s. The temperature resolution of the IR-camera was in the order of 10×10^{-3} K.

The surface temperature of the MOSFET only changes in the central area, represented by the gray to white spots in Fig. 8. The central area representing heat generation of the MOSFET is surrounded by a black colored ring, which indicates a constant temperature over the observed time frame. Generally, the flow directions of the generated heat can be vertical, from the hot spot inside the semiconductor to its surface. Due to the metal cover of the MOSFET and its high thermal conductivity the heat can also spread horizontally along the plane cover. The short time frame of the measurements reduces horizontal heat spreading and, thus, ensures the detection of hot spots. Based on these results, the injection nozzle was placed in the center position of the chamber housing.

Fig. 9 presents the experimental results of the spatially averaged heat transfer coefficient for different nozzle lengths and volume flow rates. For both nozzle lengths, the heat transfer coefficient is nearly identical.

B. Pressure Drop and Pumping Power

The thermohydraulic comparison of Robinson [1] highlights the tradeoff between pressure drop and volumetric flow rate in impinging jet applications. High volume flow rates cause high pressure drops and, thus, increase the required pumping power. Increasing the outlet velocity leads to higher local and spatially averaged heat transfer coefficients and, as a result, better cooling performance. To determine these competing effects on the cooling performance of the direct impinging jet cooling the electrically noninsulated setup (Case A) was equipped with two different nozzle lengths ($L_N = 12$ mm and $L_N = 24$ mm). For both nozzles, a flow rate variation was performed and the dissipated heat was measured. All experiments and numerical investigations were conducted under steady-state conditions, using same coolant and ambiance temperatures. Furthermore, the test setup was thermally insulated to avoid heat loss to the ambient.

Besides heat transfer characteristics and space requirements of the cooling method pumping power is an important parameter. The pumping power P depends on the pressure drop Δp and the volumetric flow rate $\dot{V}$

$$P = \dot{V} \cdot \Delta p. \tag{5}$$

To estimate the hydrodynamic characteristics numerical simulations were performed using the commercial CFD tool ANSYS Fluent. The domain of the numerical simulations based on the geometric dimensions of the first test setup included the inlet and outlet pipes as well as the entire cooling chamber. Not included were hydrodynamic losses in the pumping system and of the hoses (incoming and outgoing liquid). The thermophysical properties of the fluid used were equal to the coolant property data at 22.5 °C. The plots in Fig. 10 summarize the numerical simulation results for a nozzle length of 12 mm and 24 mm and various volume flow rates.

The evaluation of the results regarding pressure drop and pumping power highlights the influence of the volume flow rate. For both nozzle types the pressure drop increases. Pumping power, the product of pressure drop and volume flow rate, increases even more. Taking into account the moderate increase of the heat transfer coefficient in the same flow rate range (see Fig. 9), the cooling system has to be operated with relatively high pumping power to achieve only small improvements in cooling performance. Especially the additional pressure drop of the long nozzle does not lead to significant improvements of the heat transfer coefficient.

Fulfilling the requests for a compact, reliable, and cost-effective cooling system the short nozzle ($L_N = 12$ mm) offers the best performance and was chosen for the following investigations. Also, the relatively low coolant flow rate of 30 mL/min proved adequate cooling performance. Thus, the liquid distribution system can be designed with a very low pressure drop. For the flow rate of 30 mL/min the pumping power required is approximately 1 mW, which is low for a spatially averaged heat transfer coefficient of 9000 W/m$^2\cdot$ K.

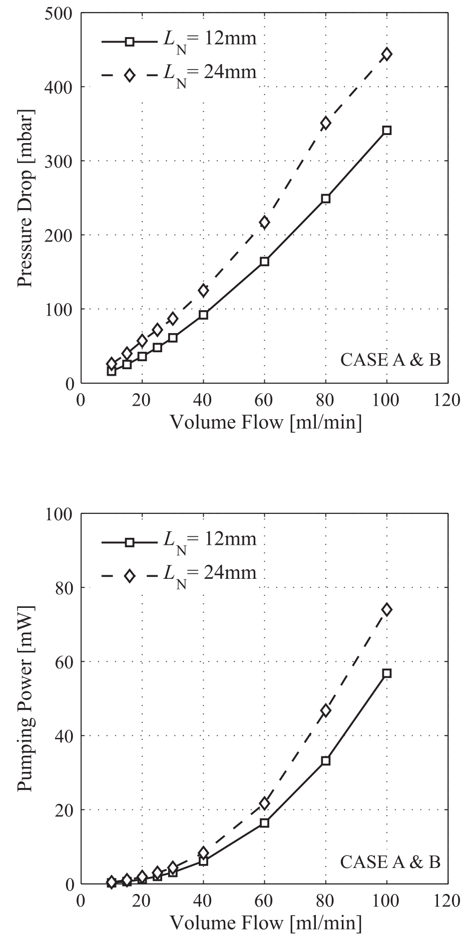

Fig. 10. Results of the numerical simulations. Upper panel: Influence of nozzle length L_N and coolant flow rate $\dot{V}$ on pressure drop Δp. Lower panel: Influence of nozzle length L_N and coolant flow rate $\dot{V}$ on pumping power P. Note: for both investigated setups (with and without electrical insulation) pressure drop and pumping power are equal.

C. Heat Transfer Characteristics

Heat transfer characteristics of the two cooling system (Case A and Case B) are experimentally obtained using the setup described in Section II.

Fig. 11 depicts the spatially averaged heat transfer coefficient $\bar{\alpha}$ in dependence of volume flow rate $\dot{V}$ and MOSFET temperature T_M. Furthermore, the influence of the electrical insulation on heat transfer is illustrated. For all experimental conditions, the electric current I_{DS} was adjusted in order to provide a constant MOSFET temperature during each flow rate variation. The drain-to-source voltage V_{DS} adjusts itself according to the MOSFET resistance, set by the gate-to-source voltage with a value of $V_{\mathrm{GS}} = 4.58$ V. Consequently, a nozzle length of $L_N = 12$ mm was chosen for all subsequent experiments and the test setup was thermally insulated. The coolant inlet temperature was $T_{\mathrm{I}} =$ 22.5 °C.

Represented by the gray line with cross marker, the development of the heat transfer coefficient of the electrically noninsulated setup (Case A) starts at a flow rate of $\dot{V} = 10$ mL/min with a value of around $\bar{\alpha} = 4250$ W/m$^2\cdot$ K, followed by a constant increase up to 8660 W/m$^2\cdot$ K at 25 mL/min. In the range of

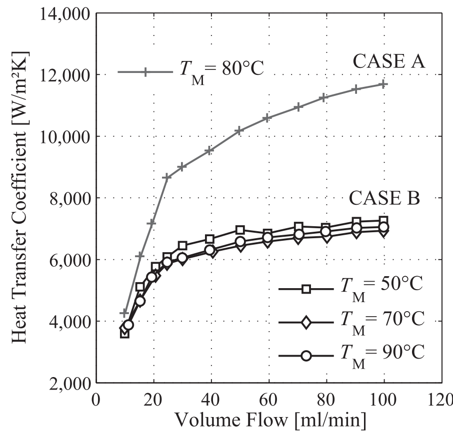

Fig. 11. Spatially averaged heat transfer coefficient of the electrically non-insulated (Case A) and electrically insulated cooling chamber (Case B). The MOSFET was operated with a gate-to-source voltage of $V_{GS} = 4.58$ V.

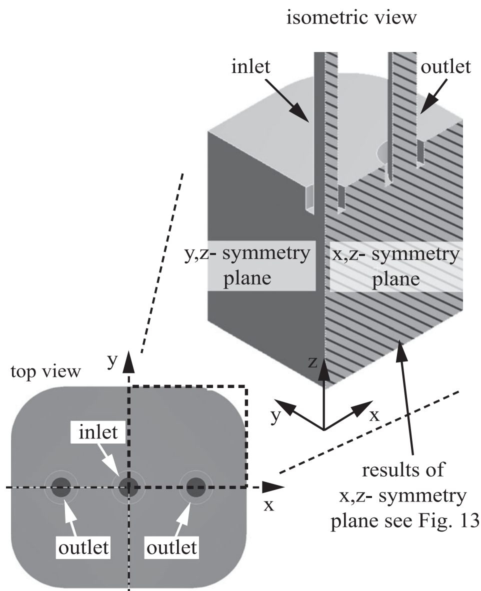

Fig. 12. Domain of the numerical investigations, as well as symmetry planes of the coolant inside the cooling chamber and nozzles.

30–100 mL/min the dependency between heat transfer coefficient and volume flow rate exhibits a square root characteristic.

With additional electrical insulation (Case B), the heat transfer coefficient is significantly lower, as illustrated by the black curves (for MOSFET temperatures of $T_M = 50$, 70, and 90 °C). All three curves have the same exponential characteristic with only minor variations in the absolute value, indicating that the temperature level does not influence the heat transfer characteristics. This suggests that forced convection is the dominant heat transfer mechanism.

Special emphasis should be drawn to the slopes of the curves in Fig. 11, which change abruptly around $\dot{V} = 25$ mL/min. This inflection point, especially prominent in Case A, indicates changing physical conditions regarding convective heat transfer and fluid dynamics in the cooling chamber.

To investigate this aspect further, numerical investigations were carried out. Fig. 12 illustrates the domain of the CFD

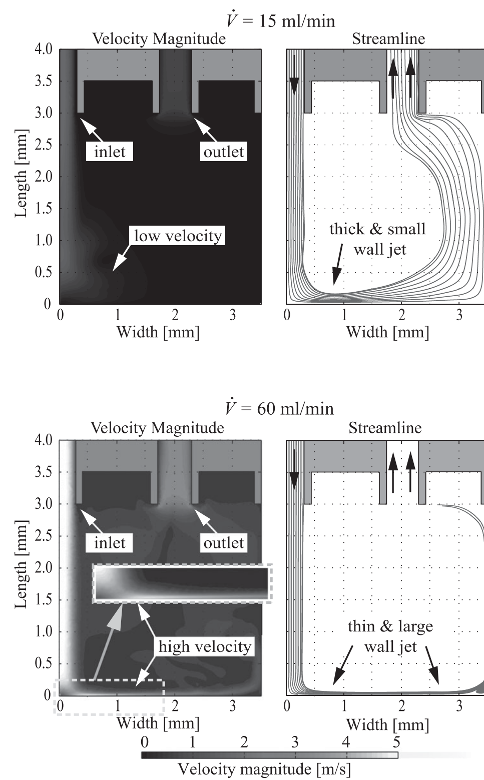

Fig. 13. Results of the numerical investigations based on the x,z-symmetry plane, highlighted green in Fig. 12. Upper panels: fluid and wall jet characteristics at a coolant flow rate of $\dot{V} = 15$ mL/min. Bottom panels: fluid and wall jet characteristics at a coolant flow rate of $\dot{V} = 60$ mL/min. The respective left panels illustrate the velocity magnitude distributions inside the cooling chamber. The respective right panels (upper and lower row) illustrate the stream lines of the coolant, beginning at the inlet nozzle.

model. Taking advantage of the symmetric design of the cooling chamber the domain represents one quarter of the liquid phase. Also, the fluid inside the inlet and outlet nozzles are included. The results of the fluid dynamics analyses are presented in Fig. 13. The results are based on the numerical results at the x, z-symmetry plane, highlighted by the cross-hatched area in Fig. 12.

Fig. 13 presents the differences of the fluid dynamics inside the cooling chamber below and beyond $\dot{V} = 25$ mL/min. The upper plots are based on a coolant flow rate of $\dot{V} = 15$ mL/min, the bottom plots on a coolant flow rate of $\dot{V} = 60$ mL/min. To evaluate the influence of the impinging jets and their corresponding wall jets on heat transfer the velocity magnitudes as well as stream lines are considered.

At a coolant flow rate of $\dot{V} = 15$ mL/min the fluid enters the cooling chamber through the inlet, gets redirected in the stagnation region (width $\simeq$ 0 mm to 0.3 mm), and develops a wall jet. As indicated by the separately observable streamlines the wall jet is of significant thickness. Along the bottom surface the thickness of the wall jet increases and, finally, turns toward the outlet nozzle. Taking into account the low fluid velocity in this area (below 1 m/s), the heat transfer is accordingly low. Increasing coolant flow rate (higher momentum of the impinging jet) increases the redirected fluid velocity in the stagnation region. The thickness of the wall jet decreases, but also, the wall

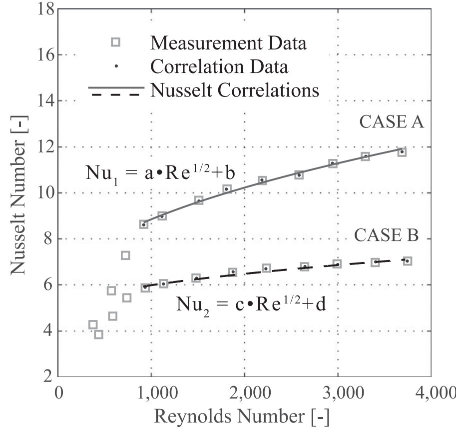

Fig. 14. Developed correlation of the Nusselt by Reynolds numbers compared to the experimental measurement data. The MOSFET temperature is adjusted to $T_M = 80\,^{\circ}$C.

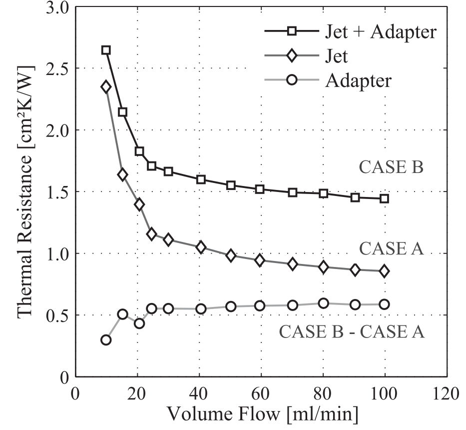

Fig. 15. Break-down of the thermal resistances for the two test setups; differentiated by their heat transfer mechanism.

jet area increases. Both effects, increasing the wall jet area as well as the wall jet velocity, result in a significant heat transfer improvement and can be obtained up to a the flow rate of $\dot{V} =$ 25 mL/min.

The bottom plots of Fig. 13 illustrate the wall jet characteristics of coolant flow rates beyond 25 mL/min. The momentum of the impinging jet is sufficient to establish the wall jet area along the entire bottom surface and decreases the wall jet thickness. The streamlines as well as the velocity distribution illustrate that the wall jet nearly reaches the cooling chamber wall ($\mathrm{width} =$ 3.5 mm). In contrast to coolant flow rates below 25 mL/min increasing the coolant flow rate leads to no further growth of the wall jet area. Thus, the development of the heat transfer coefficient beyond 25 mL/min, as observed in Fig. 11, can only be attributed to the influence of the increasing fluid velocities.

To enable scaling of the experimental results and a transfer to other cooling applications, Fig. 14 compares the dimensionless Nusselt number with classical power-law dependencies of laminar jet impingement. The Nusselt number is proportional to the Reynolds number by $\mathrm{Nu} \propto \mathrm{Re}^{1/2}$ (for more details on scaling law dependencies see [24]). The equations for the Nusselt correlations of the first ($\mathrm{Nu}_1 = f(\mathrm{Re})$) and the second setup ($\mathrm{Nu}_2 = f(\mathrm{Re})$), as well as the values of their corresponding coefficients are

$$\mathrm{Nu}_1 = a \cdot \mathrm{Re}^{1/2} + b \qquad a = 0.1052 \qquad b = 5.514 \tag{6}$$

$$\mathrm{Nu}_2 = c \cdot \mathrm{Re}^{1/2} + d \qquad c = 0.0377 \qquad d = 4.803. \tag{7}$$

Remarkably good agreement is found for Reynolds number values above $\mathrm{Re} = 800$. Below this Reynolds number, the Nusselt number increases much stronger with Reynolds number, which may indicate that the jet velocity and momentum are not sufficient to generate a fully developed wall jet on the surface of the MOSFET. As such, the area covered by the wall jet increases with Reynolds number and the Nusselt number reveals a much stronger power-law dependency on Reynolds number. Note, that critical hot spots may arise if the MOSFET is not sufficiently cooled by the wall jet. Therefore, it is recommended to operate the liquid jet impingement cooling above $\mathrm{Re} = 800$. For the given property data as well as the inlet nozzle diameter of $D = 0.6$ mm, the volume flow rate of $\dot{V} = 30$ mL/min leads to a Reynolds number of around $\mathrm{Re} = 940$.

D. Thermal Resistance

The reciprocal value of the heat transfer coefficient is the thermal resistance. This value is a good indicator to quantify the performance of the cooling device. The experimental investigations in this study comprise of two setups, with and without electrical insulation. This approach allows us to differentiate the thermal resistance of the impinging jet cooling and electrical insulation. For the test setup equipped with the electrical insulation (Case B) the thermal resistance is given by

$$R_{\mathrm{Jet+Adapter}} = R_{\mathrm{Jet}} + R_{\mathrm{Adapter}}. \tag{8}$$

In this case, the thermal resistance $R_{\mathrm{Jet+Adapter}}$ comprises the jet impingement resistance R_{Jet} and the thermal resistance of the adapter plate R_{Adapter}. Both resistances can be determined by

$$R_{\mathrm{Jet}} = \frac{1}{\bar{\alpha}_{\mathrm{Jet}}}, \qquad R_{\mathrm{Adapter}} = \frac{\delta_{\mathrm{Brass}}}{\lambda_{\mathrm{Brass}}} + \frac{\delta_{\mathrm{Insulation}}}{\lambda_{\mathrm{Insulation}}}. \tag{9}$$

The thermal resistance of the jet impingement cooling depends on the heat transfer coefficient $\bar{\alpha}_{\mathrm{Jet}}$ and, due to this, on the coolant flow rate $\dot{V}$. Thus, the thermal resistance of the electrically noninsulated setup (Case A) can be divided from the heat transfer measurements. The thermal resistance of the adapter plate depends on the heat conductivity of the electrical insulation $\lambda_{\mathrm{Insulation}}$ and brass λ_{Brass}, as well as their layer thicknesses ($\delta_{\mathrm{Insulation}}$ and δ_{Brass}).

In order to highlight the adverse effects of the electrical insulation on the heat transfer Fig. 15 illustrates the dependency of thermal resistances on coolant flow rate of the investigated cooling chambers. The thermal resistance of the cooling chamber equipped with electrical insulation (Case B) is represented by the black curve with square markers (Jet + Adapter). The thermal resistance characteristic of the cooling chamber without electrical insulation (Case A) is represented by the gray curve with diamond markers (Jet). The light gray curve with circle

markers (Adapter) of Fig. 15 represents their difference. Thus, the thermal resistance of the adapter can be determined. The thermal resistance of jet impingement decreases from $R_{\text{Jet}} =$ 2.35 cm$^2\cdot$ K/W at a volume flow rate of $\dot{V} = 10$ mL/min, down to $R_{\text{Jet}} = 0.85$ cm$^2\cdot$ K/W at a volume flow rate of $\dot{V} = 100$ mL/min. The curve of the thermal resistance representing the setup including electrical insulation (Jet + Adapter) reveals the same characteristic profile, but has higher thermal resistances. At a volume flow rate of $\dot{V} = 10$ mL/min, the thermal resistance decreases from $R_{\text{Jet+Adapter}} = 2.65$ cm^2 K/W down to $R_{\text{Jet+Adapter}} = 1.64$ cm$^2\cdot$ K/W. In contrast to the thermal resistance curves of Cases A and B, the thermal resistance of the adapter shows no apparent dependency on coolant flow rate. Except for small volume flow rates (10–25 mL/min) the value of the adapter thermal resistance is approximately $R_{\text{Adapter}} =$ 0.58 cm$^2\cdot$ K/W. Compared to the jet impingement the additionally installed electrical insulation (Case B) contributes to more than 30% on the thermal resistance of the cooling device. The layer thickness of the adapter plate $\delta_{\text{Brass}} = 0.6$ mm and electrical insulation pad $\delta_{\text{Insulation}} = 0.2$ mm, as well as the corresponding thermal heat conductivities ($\lambda_{\text{Brass}} = 120$ W/m$\cdot$ K and $\lambda_{\text{Insulation}} = 5$ W/m$\cdot$ K) lead to a thermal resistance of the adapter of $R_{\text{Adapter}} = 0.45$ cm$^2\cdot$ K/W. The difference between the measured and the calculated value of the adapter's thermal resistance can be addressed to differences in insulation thickness, but also to additional nonconsidered resistances (i.e., solder between the MOSFET surface and adapter lower surface). Taking into account the findings for pressure drop and pumping power (see Section IV-B), the maximum power distribution of the MOSFET is measured at a coolant flow rate of 30 mL/min. The required pumping power of 1 mW is low for an average heat transfer coefficient of 6170 W/m$^2\cdot$ K. Limited by the maximum MOSFET temperature of 163 °C and coolant inlet temperature of 22.5 °C, the maximum measured power distribution was 51 W. Under these conditions, the MOSFET temperature exceeded the boiling temperature of the coolant of 100 °C and steam bubbles were detected at the transparent outlet tubes. The steam bubbles collapsed before passing the mounted outlet thermocouples. This ensured reliable measurements of the thermocouples at the outlet. Also, steady-state coolant outlet temperatures were measured. The boiling conditions inside the cooling chamber did not cause instabilities of the cooling system or semiconductor. A possible explanation is the impinging liquid jet, which pushes the steam bubbles out of the cooling chamber.

E. Failure Scenario

The failure scenario is an important aspect in electrical component cooling. To evaluate the thermal response of a power electronic control unit the temporal temperature rise of the MOSFET in the case of a coolant supply shutdown is presented. The MOSFET was operated under steady-state conditions and the inlet pipe was blocked. Before shutdown, the cooling device was supplied with a constant coolant flow rate of $\dot{V} = 30$ mL/min at an inlet temperature of $T_{\text{I}} = 22.0$ °C. The electrically insulated second setup was chosen because it is the more application-oriented and it also reflects the worst case scenario. The measurement result are presented in Fig. 16.

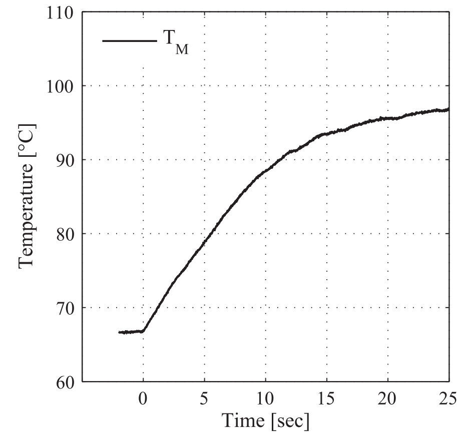

Fig. 16. Failure scenario: Shut down of the coolant flow at $t = 0$ s. Tracking of the MOSFET temperature at a power distribution of approximately 11.0 W and an inlet temperature of $T_{\text{I}} = 22.0$ °C.

The MOSFET temperature was continuously tracked (steady-state value of $T_M = 67$ °C), while the semiconductor was operated with a power loss of approximately 11.0 W. The results in Fig. 16 show that the coolant supply shutdown leads to an immediate temperature rise with a gradient of around $dT_M/dt =$ 3 k/s within the first seconds. After approximately $t = 25$ s, the MOSFET temperature reaches the maximum value of $T_M =$ 97 °C. To prevent any damage of the MOSFET and boiling of the coolant the power supply was switched OFFat this point.

The square root progress of the temperature curve can be explained by the thermal inertia of the test setup, but also by the temperature sensitivity of the MOSFET. With increasing temperature the ohmic resistance of the MOSFET decreases along with its heat generation. At the beginning of the coolant shutdown, the heat generation was 11.0 W; at $t = 25$ s, the power generation was reduced to 3.0 W.

Due to the heat capacities of the cooling chamber, the inside remaining coolant, and the convective heat loss to the ambiance the temperature rise is moderate. However, the time period of several seconds, until a significant temperature rise is detected, is sufficient for an adequate response of a control unit. Under shutdown conditions steam bubbles cannot be removed. This may cause pressure rise and thus, damage to the cooling chamber if the temperature rises above 100 °C. Thus, in order to prevent boiling of the water inside the cooling chamber the MOSFET was operated up to a maximum temperature of $T_M = 100$ °C.

F. Efficiency

To evaluate the efficiency of the impinging jet cooling, Fig. 17 compares the required pumping power to the heat transfer coefficient. In general, the heat removal rate of the cooling depends on the temperature difference between the coolant inlet temperature and surface temperature, as well as on the heat transfer coefficient. In common applications, the coolant inlet temperature is restricted by the cooling cycle and its conditioning system. The heat transfer coefficient correlates with the coolant flow rate, which is determined by the pumping power. Characterizing the system efficiency by the required pumping power and

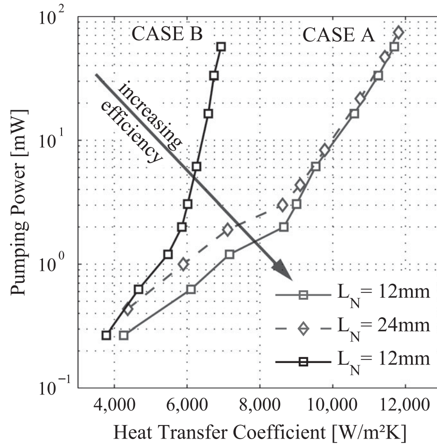

Fig. 17. Results of the numerical and experimental investigations to evaluate the efficiency of the impinging jet cooling approaches (of the electrically noninsulated (Case A) and electrically insulated cooling chamber (Case B)) using nozzle lengths ranging between 12 and 24 mm. Comparison of the required pumping power P (numerical results) with respect to the achieved heat transfer coefficients $\bar{\alpha}$ (experimental results).

heat transfer coefficient allows for a temperature-independent evaluation of the cooling performance.

Fig. 17 illustrates the influence of the nozzle length on the efficiency. In the range of $\bar{\alpha} = 4300\ \mathrm{W/m^2{\cdot}K}$ to $8600\ \mathrm{W/m^2{\cdot}K}$ the nozzle with a length of $L_N = 24$ mm requires more pumping power to achieve the same heat transfer coefficients compared to the nozzle with a length of 12 mm. Reducing nozzle length increases the efficiency of the impinging jet cooling approach. The numerical investigations proved that the nozzle length of 12 mm (with a nozzle diameter of 0.6 mm) is sufficient to develop parabolic velocity profiles at the inlet. Beyond the heat transfer coefficient of $\bar{\alpha} = 8600\ \mathrm{W/m^2} \cdot \mathrm{K}$ no efficiency benefits of the short nozzle can be obtained.

Furthermore, Fig. 17 highlights the efficiency drawback of the additionally installed electrical insulation (TIM). The required pumping power of the investigated cases [electrically noninsulated (Case A) and electrically insulated cooling chamber (Case B)] using the inlet nozzle with a length of $L_N = 12$ mm is in the same range. Due to the additional thermal resistance of the TIM, the heat transfer coefficients of Case B are smaller. This leads to a significant reduction of the cooling efficiency in Case B compared to the efficiency of the electrically noninsulated cooling approach in Case A.

V. Conclusion

In this paper, a new approach of direct liquid cooling of a MOSFET semiconductor with a single impinging jet was presented. The cooling concept focused on hot spot removal and the reduction of thermal resistances. The design of the coolant chamber and the positioning of the nozzle center was based on IR-thermography measurements of the spatial temperature distribution of the MOSFET, illustrating the hot spots of the semiconductor. Two different concepts, with and without electrical insulation between the MOSFET and the coolant chamber were tested. The TIM material with a thickness of merely 200 μm was found to significantly contribute to the total thermal resistance (30% and more). Omitting an electrical insulation sets special requirements to the cooling liquid. The dimensionless heat transfer coefficient (Nusselt number) was found to increase with flow rate (or Reynolds number) in two different regimes. For higher flow rates ($1000 < \mathrm{Re} < 4000$), the classical power-law dependency for laminar jet impingement was found to be well-suited for the prediction of the cooling performance. For lower flow rates ($\mathrm{Re} < 1000$), the Nusselt number increased much stronger with Reynolds number. Besides the experimental analysis of the heat transfer characteristics the results of numerical simulations provided insights into fluid dynamics and wall jet development inside the cooling chamber, as well as its influence on the heat transfer. Numerical investigations of pressure drop and pumping power reflected the relatively low energy requirements in terms of pumping power to achieve sufficient cooling performances.

The experimental and numerical investigations of the heat transfer characteristics and cooling performances illustrate the potential of direct impinging jet cooling. Even for small coolant flow rates the cooling concept achieved adequate heat transfer coefficients and heat dissipation rates. The compact design of the injection chamber and its attachment to the MOSFET top cover minimize the thermal resistance. To fulfill the requirements of future applications further improvements of the heat transfer coefficient of impinging jets should be achieved. For example, the number of impinging jets could be increased and the bottom chamber surface could be equipped with microfins. Furthermore, lower thermal resistance of the TIM could increase the heat removal rates of the cooling chamber.

The present cooling approach offers the opportunity of individual cooling of heat dissipating components of power electronic modules, such as MOSFETs or IGBTs. Due to separately installed cooling chambers, new flexibility in design of PCBs and DCBs can be realized. Their layout is no longer restricted by a planar heat sink. Also, nonhomogeneous heat conductivity between each MOSFET and the heat sink can be avoided. Furthermore, the achieved high heat transfer coefficients allow further reduction of the coolant flow rate. This leads to higher coolant outlet temperatures, which offers benefits on the heat removal of cooling cycle to the ambiance, and thus, offers additional potential for downsizing.

References

[1] A. J. Robinson, "A thermal-hydraulic comparison of liquid microchannel and impinging liquid jet array heat sinks for high-power electronics cooling," *IEEE Trans. Compon. Packag. Technol.*, vol. 32, no. 2, pp. 347–357, Jun. 2009.

[2] S. Kang, "Advanced cooling for power electronics," in *Proc. Int. Conf. Integr. Power Electron. Syst.*, Nuremberg, Germany, Mar. 2012, pp. 8–8.

[3] V. Benda, "Power semiconductors—State of the art and future trends," *Global J. Technol. Optim.*, vol. 2, pp. 29–36, Jan. 2011.

[4] J. Vobecky, "Future trends in high power devices," in *Proc. Int. Conf. Microelectron.*, Niš, Serbia, May 2010, pp. 16–19.

[5] J. Biela, M. Schweizer, S. Waffler, B. Wrzecionko, and J. W. Kolar, "SiC vs. Si—Evaluation of potentials for performance improvement of power electronics converter systems by SiC power semiconductors," *IEEE Trans. Ind. Electron.*, vol. 58, no. 7, pp. 2872–2882, Jul. 2011.

[6] J. Schulz-Harder, "Review on highly integrated solutions for power electronic devices," in *Proc. 5th Int. Conf. Integr. Power Syst.*, Nuremberg, Germany, Mar. 2008, pp. 1–7.

[7] D. Saums, "Vehicle electrification thermal management challenges and solutions overview," in *Proc. MEPTEC Therm. Manage. Workshop*, San Jose, CA, USA, Mar. 2011.

[8] S. G. Leslie, "Cooling options and challenges of high power semiconductors," *Electron. Cooling*, vol. 12, no. 4, pp. 20–27, Nov. 2006.
[9] J. Valenzuela, "Liquid cooling for high-power electronics," *Power Electron. Technol.*, vol. 31, pp. 50–56, Feb. 2005.
[10] J. C. Howes, D. B. Levett, S. T. Wilson, J. Marsala, and D. L. Saums, "Cooling of an IGBT drive system with vaporizable dielectric fluid (VDF)," *Twenty-fourth Annu. IEEE Semicond. Thermal Meas. Manage. Symp.*, pp. 9–15, Mar. 2008.
[11] B. W. Webb and C. F. Ma, "Single-phase liquid jet impingement heat transfer," *Adv. Heat Transf.*, vol. 27, no. 17, pp. 105–217, 1995.
[12] J. H. Lienhard, "Liquid jet impingement," *Annu. Rev. Heat Transf.*, vol. 6, pp. 199–270, 1995.
[13] S. V. Garimella, "Heat Transfer and flow fields in confined jet impingement," *Annu. Rev. Heat Transf.*, vol. 6, pp. 413–494, 2000.
[14] D. J. Womac, S. Ramadhyani, and F. P. Incropera, "Correlation equations for impingement cooling of small heat sources with single circular liquid jets," *ASME J. Heat Transf.*, vol. 115, pp. 106–115, 1993.
[15] D. J. Womac, F. P. Incropera, and S. Ramadhyani, "Correlation equations for impingement cooling of small heat sources with multiple circular liquid jets," *ASME J. Heat Transf.*, vol. 116, pp. 482–486, 1994.
[16] D. C. Wadsworth and I. Mudawar, "Cooling of a multichip electronic module by means of confined two-dimensional jets of dielectric liquid," *ASME J. Heat Transf.*, vol. 112, pp. 891–898, 1990.
[17] T. Brunschwiler *et al.*, "Direct liquid jet-impingement cooling with micronsized nozzle array and distributed return architecture," in *Proc. Intersoc. Conf. Thermomech. Phenom. Electron. Syst.*, 2006, pp. 693–699.
[18] S. Narumanchi, M. Mihalic, G. Moreno, and K. Bennion, "Design of light-weight, single-phase liquid-cooled heat exchanger for automotive power electronics," in *Proc. Intersoc. Conf. Therm. Thermomech. Phenom. Electron. Syst.*, 2012, pp. 693–699.
[19] Y. Han, B. L. Lau, G. Tang, X. Zhang, and D. M. W. Rhee, "Si-based hybrid microcooler with multiple drainage microtrenches for high heat flux cooling," *IEEE Trans. Compon., Packag., Manuf. Technol.*, vol. 7, no. 1, pp. 50–57, Jan. 2017.
[20] K. Gould, S. Q. Cai, C. Neft, and A. Bhunia, "Liquid jet impingement cooling of a silicon carbide power conversion module for vehicle applications," *IEEE Trans. Power Electron.*, vol. 30, no. 6, pp. 2975–2984, Jun. 2015.
[21] S. Narumanchi, M. Mihalic, and K. Kelly, "Thermal interface materials for power electronics applications," in *Proc. IEEE Intersoc. Therm. Thermomech. Phenom. Electron. Syst.*, Sep. 2008, pp. 395–404.
[22] J. Schulz-Harder, K. Exel, and A. Meyer, "Direct liquid cooling of power electronics devices," in *Proc. 4th Int. Conf. Integrated Power Syst.*, Naples, Jun. 2006, pp. 1–6.
[23] G. Engelmann, T. Senoner, H. van Hoek, and R. W. De Doncker, "A systematic comparison of various thermal interface materials for applications with surface-mounted (DirectFET^{TM}) MOSFETs," in *Proc. IEEE 11th Int. Conf. Power Electron. Drive Syst.*, 2015, pp. 112–117.
[24] W. Rohlfs, C. Ehrenpreis, H. D. Haustein, O. Gabrecht, and R. Kneer, "Influence of the local flow acceleration on the heat transfer of submerged and free-surface jet impingement," in *Proc. Int. Heat Transf. Conf.*, Kyoto, Japan, 2014, pp. 3179–3192.
[25] International Rectifier, "DirectFET^{TM} Power MOSFET Datasheet," Feb. 2014. [Online]. Available: www.irf.com
[26] Electronics Group of Henkel: Bergquist Company, "Gap PAD 5000S35 datasheet," Mar. 2016. [Online]. Available: www.bergquistcompany.com

Johannes Jörg received the Master's degree (Dipl.-Ing.) in mechanical engineering specialized in energy engineering from the RWTH Aachen University, Aachen, Germany, in 2013.

Since 2013, he has been a participant of the mobilEM Graduate School and working as a Research Assistant in the Institute of Heat and Mass Transfer, Aachen, Germany. He contributes to the development of contactless temperature measurement systems. His research interest includes convective heat transfer focused on impinging microjet cooling and jet interaction.

Silvano Taraborrelli (S'16) received the Master's degree (Laurea) in electrical engineering from the Politecnico di Torino, Turin, Italy, in 2010.

Since 2012, he has been working as a Research Assistant in the Institute for Power Electronics and Electrical Drives, RWTH Aachen University, Aachen, Germany, in the Power Electronic Group. Since 2013, he has been a participant of the mobilEM Graduate School. His research interests include dc–dc converter with wide voltage range for automotive application.

Garikoitz Sarriegui received the B.Sc. and M.Sc. degrees in automatization and industrial electronics from the University of Mondragon, Mondragon, Spain, in 2007 and 2010, respectively. He is currently working toward the Ph.D. degree in SiC and GaN semiconductors at RWTH Aachen University, Aachen, Germany.

Since 2011, he has been a Research Associate in the Institute for Power Electronics and Electrical Drives, RWTH Aachen University. His current research interests include power electronic converter design and implementation, and wide bandgap semiconductor devices.

Rik W. De Doncker (M'87) received the Ph.D. degree in electrical engineering from the Katholieke Universiteit Leuven, Leuven, Belgium, in 1986.

In 1987, he was appointed as a Visiting Associate Professor at the University of Wisconsin, Madison. After a short stay as an Adjunct Researcher with Interuniversity Microelectronics Centre, Leuven, he joined, in 1989, the Corporate Research and Development Center, General Electric Company, Schenectady, NY. In 1994, he joined Silicon Power Corporation, a former division of General Electric, Inc., as the Vice President of technology. In 1996, he became a Professor at RWTH Aachen University, Aachen, Germany, where he currently leads the Institute for Power Electronics and Electrical Drives. Since 2006, he has been the Director of the E.ON Energy Research Center, RWTH Aachen University.

Dr. De Doncker was the President of the IEEE Power Electronics Society (PELS) in 2005 and 2006. He was the founding Chairman of the German IEEE Industry Applications Society PELS Joint Chapter. In 2002, he received the IEEE IAS Outstanding Achievement Award. In 2008, he received the IEEE PES Nari Hingorani Custom Power Award. In 2009, he led a VDE/ETG Task Force on Electric Vehicles. In 2010, he received an honorary doctor degree of TU Riga, Latvia. In 2013, he received the IEEE William E. Newell Power Electronics Award.

Reinhold Kneer received the Doctoral degree (Dr.-Ing.) in mechanical engineering specialized in atomization processes in combustion engines from the Karlsruhe Institute of Technology, Karlsruhe, Germany, in 1994.

Since 2004, he has been the Head of the Institute of Heat and Mass Transfer, RWTH Aachen University, Aachen, Germany. The Institute of Heat and Mass Transfer focuses on fundamental research projects on the basis of transport processes, boundary layer processes, and phase changes.

Wilko Rohlfs received the Diploma in mechanical engineering in 2009 and the Ph.D. degree in 2015. In 2014 he received his PhD in economics from RWTH Aachen University.

He is currently a Researcher and Leader of the research group "Convective Transport Processes" at the Institute of Heat and Mass Transfer, RWTH Aachen University, Aachen, Germany. His major research topics in fluid dynamics are falling liquid films and jet impingement.